Laboratory simulation of space weathering on silicate surfaces in water environment

Mara Murri, Giancarlo Capitani, Mauro Fasoli, Angelo Monguzzi, Alberto Calloni, Gianlorenzo Bussetti, Nadia Malaspina, Marcello Campione*

ABSTRACT

Silicate nanoparticles occur in various astrophysical environments where they experience substantial processing due to events such as grain-grain collisions and irradiation. However, the structure and chemical evolution together with the origin of these grains are still poorly understood and intensively debated. For this purpose, we performed liquid-phase nanosecond pulsed laser ablation on olivine single crystals to (i) simulate space weathering in a water environment (e.g., hydrous or volatile-rich bodies) and (ii) study the chemical and structural evolution of both the target surface and the ablated material. In particular, optical spectroscopy analyses have been performed on the ablated material and correlated with high-resolution transmission electron microscopy and diffraction; whereas, compositional variations of the ablated target surface were determined by X-ray photoelectron spectroscopy. Our results show that the target material is

1

19   enriched in Fe and depleted in Mg after the ablation process, with the water environment triggering

20   the oxidation of Fe^{2+} into Fe^{3+} in a region confined at the solid-liquid interface and thus promoting

21   the formation of magnetite on the sample surface. On the other hand, in the ablated material we

22   find olivine crystalline fragments with shock features together with Mg-rich crystalline

23   nanoparticles. Notably, no metallic iron nanoparticles have been detected in the ablated material.

24   Our simulation of space weathering in water environment revealed structural and chemical

25   changes which are expected to give rise to distinctive features in the reflectance spectra when

26   compared to those from airless bodies of the inner Solar System.

27   GRAPHICAL ABSTRACT

28

29

30

2
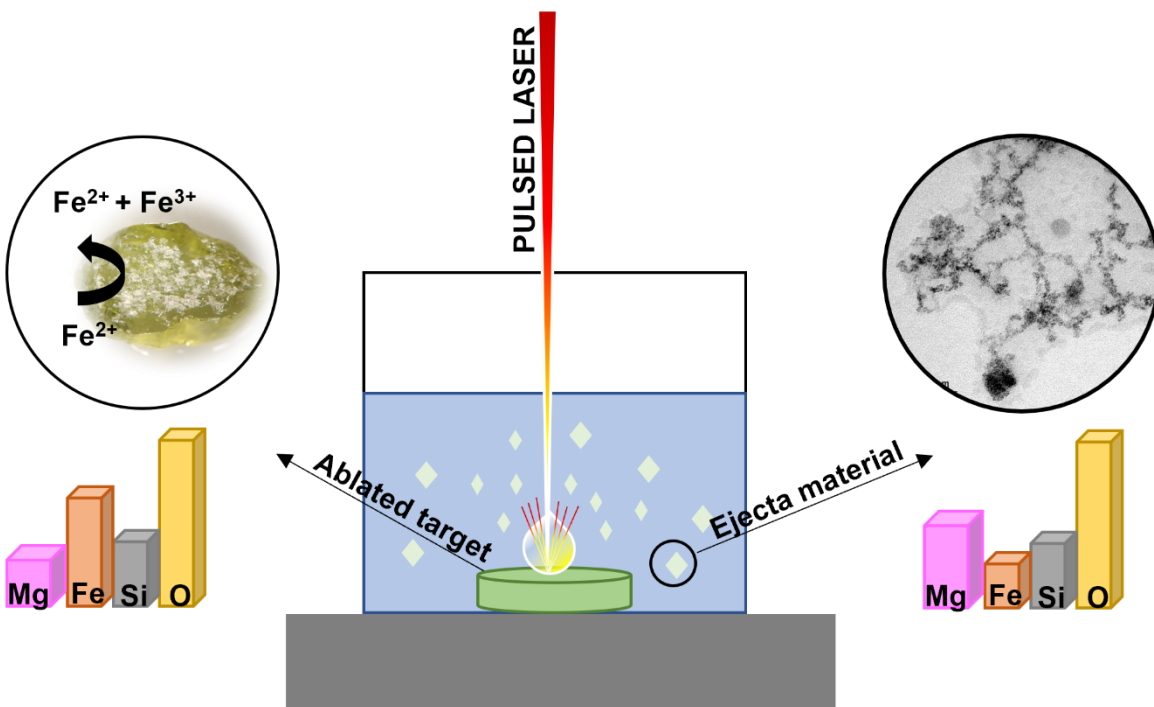
INTRODUCTION

Dust grains occur in various astrophysical environments (i.e., from comets to the farthest known galaxies) being the major responsible of a large variety of processes in the interstellar medium [1,2]. Indeed, thanks to their high surface-to-volume ratio, they act as catalytic substrates for the formation of common and complex molecules and their structure (i.e., crystalline or amorphous), size and shape, play a fundamental role in the surface reactivity [3,4]. In particular, according to ref [5], interstellar grains are divided into three main size domains in accordance with the ranges 1000-100 nm, 100-5 nm, and 5-0.3 nm. In the context of materials science and engineering, particles with a size included in the last two ranges are referred to as nanoparticles, a term used to indicate a substantial distinction of the material properties with respect to those of the bulk phase. Furthermore, particles with a size included in the last range are also usually referred to as Very Small Grains (VSGs), in accordance with the terminology employed in planetary sciences. VSGs are those with the highest relative abundance among interstellar grains.

Among dust grains, the silicates are the most common species [6,7]. The existence of interstellar silicate grains was first proposed by Kamijo in 1963 [8] and a few years later they were detected in several cosmos regions. The broad infrared (IR) feature detected around 10 μm corresponding to the Si-O stretching mode suggests that most silicate grains in the interstellar medium are amorphous. However, the new advanced spectrometers coupled with the development of the Infrared Space Observatory (ISO) revealed the presence of crystalline silicates around comets, dust disks and in interplanetary dust particles (see ref [9] and references therein). These grains experience a strong structural modification during their lifetime in the diffuse interstellar medium due to events such as grain-grain collisions and irradiation. Grain amorphization is one of the major effects, transforming crystalline silicate grains concentrated in star envelopes into

54 amorphous material populating the interstellar medium [10]. However, after the amorphization

55 process, residual crystalline features could be still retained giving rise to a population of crystalline

56 silicate nanoparticles occurring in the interstellar regions [11]. Moreover, it cannot be ruled out also

57 the possibility that the crystalline size domains of the nanoparticles are below the detection limit

58 of the available spectroscopic techniques.

59 The main building blocks of the interstellar silicates are O, Si, Fe, Mg, Al and Ca; all

60 elements that are among the principal constituents of the Earth's surface [12], thus leading to the

61 name "astronomical silicates". Moreover, the comparison of acquired IR spectra with laboratory

62 ones provided the necessary information to confirm that astronomical silicates have mainly olivine

63 and pyroxene composition [7,11,13,14].

64 The persistent space weathering processes these astronomical silicate grains experience in

65 the outer space (e.g., from irradiation, ion bombardment to impact shock events) might cause also

66 irreversible chemical changes [15]. These changes are still poorly understood and characterized given

67 the difficulties in reproducing the pertinent atmospheres and environments and the limited

68 instrumental resolution of remote sensing data. However, understanding the effects of these

69 processes is of fundamental importance (i) for the correct interpretation of remote sensing data and

70 (ii) to increase the knowledge on nanoparticles vs bulk material properties [7].

71 For this purpose, space weathering processes have always been the subject of experimental

72 and theoretical studies [1,15-19] aimed at simulating the physical and optical properties of interstellar

73 dust grains and the surface alteration of planetary bodies [4,10,11,20-23]. In particular, irradiation with

74 high energy ions (e.g., H^+, He^+), nano- and femtosecond pulsed laser ablation have been carried

75 out in vacuum on selected silicate samples (e.g., powder, single crystals, pellets) to reproduce the

76 effects of solar wind radiation and shock events on airless bodies [10,16,17,22,24-26].

77   Furthermore, hydrous or volatile-rich bodies with distinct amounts of H and OH such as

78   Vesta, Ceres, are also subjected to space weathering processes [15,27-30]. However, these bodies,

79   despite being airless, do not exhibit a measurable content of metallic iron particles on their surface.

80   This evidence has been attributed to a lesser flux of solar wind and meteoroid bombardment with

81   respect to Moon or Mercury [15,29]. Moreover, dust/ice agglomerates are known to populate dense

82   molecular clouds, comets and planet-forming disks (e.g., evidence from samples returned by the

83   Stardust mission [31] and data obtained from the Rosetta mission [32]). For examples, the recent results

84   by Potapov et al. [33,34] showed that silicate grains can entrap water ice molecules at 8 K giving rise

85   to stable silicate agglomerates mixed with ice up to 200 K when the water molecules start to desorb.

86   Even though space weathering processes are receiving more and more attention, the role

87   of volatile species in space weathering together with the structural-chemical evolution and the

88   origin of these cosmic silicates are still poorly understood and intensively debated [7,30,35].

89   Therefore, the aim of this study is the experimental simulation of space weathering

90   processes by liquid-phase nanosecond pulsed laser ablation (LP-PLA) on olivine single crystals to

91   shed light on the structure and chemical evolution of both the impacted silicate target and the

92   ejected/ablated material in a water environment.

93   Laser ablation is usually performed in vacuum or inert atmosphere, but an alternative

94   configuration was proposed by Patil et al. [36] where the target is immersed in a liquid medium, and

95   the high intensity laser beam is focused through the liquid onto the surface of the target. This

96   procedure is also widely used to synthesize nanoparticles in a clean environment with respect to

97   chemical synthesis methods, thus providing several advantages in both laboratory and industrial

98   applications [37,38]. In LP-PLA, the interaction of the high intensity laser pulse with the target surface

99   produces an ablation plume of ejected material, in which the surface of the solid target and a small

100 amount of the surrounding liquid are vaporized to form bubbles until they collapse with substantial

101 increment of the cooling rates with respect to air or vacuum, giving rise to products in the form of

102 nanoparticles suspended within the liquid medium. This allows either for their simple retrieval by

103 filtration and evaporation of the liquid, or for their further laser processing [39]. The tamping effect

104 of the liquid layer allows for the control of the ablation rate while incrementing local pressure,

105 with some advantages in terms of control of nanoparticle size distribution, shape and structure [40,41].

106 On the other side, the remnant target represents a useful product of the extreme conditions induced

107 during the plasma recoil effects (laser peening).

108 This work has been carried out by means of a multiple technique characterization in order

109 to investigate the chemical-physical properties of both the shocked target surface and the ablated

110 nanoparticles. X-ray Photoelectron Spectroscopy (XPS) analyses have been carried out to analyze

111 the surface chemical composition and speciation of the target material before and after laser

112 treatment. High-resolution transmission electron microscopy (HR-TEM) coupled with optical

113 spectroscopy and dynamic light scattering measurements have been performed on colloidal

114 solutions of the ablated nanoproducts. Analyses of their electrostatic properties and acid/base

115 reactivity have been also carried out for a deeper chemical characterization. Our results show that

116 a substantial chemical processing might be expected in both interstellar grains and silicate surfaces

117 during space weathering processes in water environments, having distinctive features with respect

118 to space weathering occurring in vacuum environment. This study provides also additional tools

119 for (i) the identification of grains of different origin by means of distinctive features in the

120 reflectance spectra (e.g., presence or absence of reddening phenomena) and (ii) the comprehension

121 of the cosmic evolution of dust particles with particular emphasis on the role of water.

122

123 METHODOLOGY

124   The olivine crystals of this study (average size $5\times4\times3$ mm^3 up to 1 cm for the longest

125   direction) were sampled along the Mosteiros beach (São Miguel island, Azores) from basaltic and

126   pyroclastic deposits of the Sete Cidades volcano. The Sete Cidades volcano lithologies spread from

127   basaltic to trachytic passing from the pre-caldera to the caldera-forming phase and the post caldera

128   (see ref [42]). The mafic rocks are classified as alkali-basalts and mainly contain phenocrysts of

129   olivine, clinopyroxene and plagioclase in a fine-grained matrix. Olivine phenocrysts of mm size

130   show euhedral shapes, a pale green color and their transparency is often reduced by the presence

131   of inclusion phases such as spinel, plagioclase and ilmenite [42].

132   A set of three Mosteiros olivine crystals has been selected for chemical analyses by

133   Scanning Electron Microscopy (SEM) Energy Dispersive X-ray Spectroscopy (EDS) to evaluate

134   the homogeneity of the bulk chemistry and the mineral chemistry of the inclusion phases. Whereas

135   another olivine crystal has been analyzed using Synchrotron Mössbauer spectroscopy to explore

136   the possible occurrence of Fe^{3+} in the target material. Pulsed laser ablation was performed on one

137   single crystal of olivine and high-resolution transmission electron microscopy followed by optical

138   absorption spectroscopy, dynamic light scattering and ζ-potential analyses were performed on the

139   resulting ablated material (see supporting info for more details about the dynamic light scattering

140   and ζ-potential measurements). XPS measurements were carried out in parallel on another olivine

141   crystal in order to evaluate the chemical composition variations before and after the ablation

142   process.

143   **Scanning Electron Microscopy**

144   The three selected crystals were embedded in epoxy and carbon coated for the SEM- EDS

145   analyses. The concentrations of major elements and, in some cases, NiO were measured by means

146 of a Zeiss Gemini 500 instrument operating at 20 keV and equipped with a Bruker QUANTAX

147 energy dispersive/wavelength dispersive detector.

148

149 **Synchrotron Mössbauer Spectroscopy**

150 Synchrotron Mössbauer spectroscopy was performed at the Nuclear Resonance Beamline

151 ID18 [43], European Synchrotron Radiation Facility (Grenoble, France) using the setup reported by

152 Potapkin et al. [44]. Room temperature Mössbauer spectra at the core and at the rim were collected

153 on one Mosteiros olivine ($0.5 \times 0.5 \times 0.3$ mm^3). The experiments were carried out at ambient

154 conditions with Be lenses and at velocities of ± 5 mm s^{-1} calibrated using a 25 μm thick natural α-

155 iron foil. The X-ray beam-size was 9×4 μm^2. The linewidth was controlled before and after each

156 sample measurement using $K_2Mg^{57}Fe(CN)_6$, whose Mössbauer spectrum consists of a single line.

157 The data were then fitted with the software MossA using the full transmission integral and a

158 Lorentzian-squared source line shape [45].

159

160 **Liquid phase nanosecond pulsed laser ablation**

161 One olivine single crystal was selected for the LP-PLA experiment and it was placed at the

162 bottom of a polystyrene box filled with 4 ml of deionized water (type 1) to immerge it completely,

163 with the liquid level at ca. 3 mm above it. LP-PLA experiments were performed with a Nd:YAG

164 laser at 1064 nm focused via a singlet lens onto the surface of the target and operating at 5 ns and

165 10 mJ per pulse with a repetition rate of 10 Hz. The ablation experiment was performed by

166 manually moving the sample to perform a laser raster scan of the sample surface. In this procedure

167 multiple laser ablations on the same spot might occur. The ablation duration was of about 10 hours.

168

X-ray photoelectron spectroscopy

XPS analyses were carried out at the Physics Department of the Politecnico di Milano on an olivine single crystal before and after the ablation. XPS measurements were performed in an ultrahigh-vacuum system (the base pressure was in the low 10^{-10} Torr range) equipped with a 150 mm hemispherical analyzer from SPECS GmbH operating at a pass energy of 20 eV [46]. Photoelectrons were excited by Al-Kα radiation (1486.6 eV), yielding an overall full width at half-maximum resolution of about 1 eV. The emitted electrons were collected at normal emission with the sample kept at room temperature. Wide energy scans and detailed scans on selected core level lines expected for the most abundant chemical species in the olivine structure (i.e., Si, Mg and Fe) were acquired.

Optical absorption spectroscopy

Absorption measurements on the colloidal solution have been carried out in the range 200-1100 nm (6.20 eV - 1.13 eV) and compared against reference colloidal solutions dispersed in deionized water (i.e. mesoporous silica [SiO_2] nanoparticles, brucite [$Mg(OH)_2$] nanoparticles, aluminum hydroxide [$Al(OH)_3$] nanoparticles, chrysotile [$Mg_3Si_2O_5(OH)_4$] nanotubes, and synthetic forsterite [Mg_2SiO_4] nanoparticles). Moreover, additional absorption analyses have been carried out as a function of the addition of known aliquots of sulfuric acid to study the suspensions behavior as a function of pH.

Electrodeposition and transmission electron microscopy

High-resolution transmission electron microscopy (HR-TEM) and EDS analyses were performed on the ablated nanoparticles deposited (i) directly from water suspension (2μl) and (ii)

192 via electro deposition of the dried water suspension re-dispersed in ethanol (applied voltage: 20 V,

193 electrode separation: 1 cm, duration: 20 minutes) onto C-coated Cu grids fixed by polypropylene

194 clamps on 1×1 cm^2 indium-tin-oxide (ITO)-coated glass plates. TEM analyses have been

195 performed with a JEOL JEM 2100Plus instrument at the Microscopy Platform of the University

196 of Milano-Bicocca. The instrument is equipped with a 9 MP Gatan Rio CMOS camera for image

197 acquisition and an Oxford EDS system for chemical analysis. The instrument was operating at 200

198 kV with a LaB$_6$ source. Image processing was carried out using the GATAN Digital Micrograph

199 software. In particular, direct measurement of the reflections from the selected area electron

200 diffraction (SAED) patterns, processing of the SAED patterns using the DiffTools [47] and the direct

201 measurement from the high-resolution bright field images coupled with the Fast Fourier Transform

202 (FFT) have been performed in order to determine the interlayer spacings of crystalline

203 nanoparticles and fragments.

204

205 RESULTS

206 **Scanning electron microscopy analyses and Synchrotron Mössbauer spectroscopy**

207 The olivine crystals from the "Mosteiros suite" are forsterite-rich [~Fo$_{87}$; (Mg$_{1.74}$, Fe$_{0.26}$)

208 SiO$_4$] and contain plagioclase (NaAlSi$_3$O$_8$-CaAl$_2$Si$_2$O$_8$) and ilmenite (FeTiO$_3$) as inclusions

209 phases. The FeO content for all the samples is constant and around 13 wt% (see Table S1), while

210 Fe^{3+} was not detected by Synchrotron Mössbauer spectroscopy (Figure S1) and Ni concentration

211 is around 1300 ppm. These results are in agreement with chemical data reported by Beier et al. [42]

212 on Azores olivines from the pre-caldera stage.

213

214 **X-ray photoelectron spectroscopy**

215   Wide XPS spectra of olivine before and after the ablation process are reported in Figure 1

216   with the main photoemission features from Fe, Si, Mg and O highlighted. Detailed scans of the

217   Fe $2p$, Si $2p$ and Mg $2s$ energy regions before and after the ablation process are reported in Figure

218   2. The binding energy scale is corrected by setting the binding energy (E_B) position of the C $1s$

219   peak from adventitious carbon to E_B= 284.8 eV as in Dukes et al. [20]. In Figure 2, the photoemission

220   spectra are normalized to the intensity of the Si $2p$ lineshape.

221   After the ablation process, a drop in the Mg intensity is clearly visible in Figure 1 (consider,

222   for instance, the signal from the Mg $1s$ and Mg Auger lines). Consistently, the relative intensity of

223   the Mg $2s$ signal decreases in Figure 2b concomitant to an increase of the relative intensity of the

224   Fe signal (Figure 2a). The binding energy positions of the photoemission features of Figure 2 are

225   in agreement with the literature[20] and we can exclude the presence of metallic Mg, Si and Fe on

226   the sample surface since that XPS spectra show no signals related to these phases. The Fe $2p$

227   lineshape (Figure 2a) changes upon ablation, with a shift of the main photoemission peaks towards

228   higher binding energy and the disappearance of the charge transfer screening structure

229   (characterized by a satellite peak at about 715.5 eV [48-50] related to the presence of Fe^{2+} ions in the

230   olivine matrix). This observation, together with the absence of any characteristic satellite structure,

231   points towards a partial oxidation of Fe^{2+} into Fe^{3+} upon ablation, consistent with the formation of

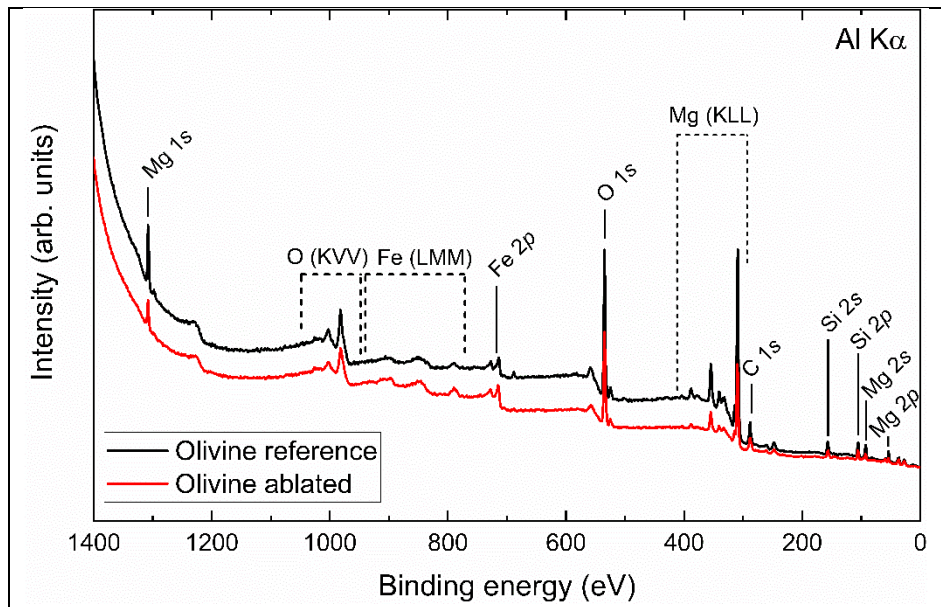232   magnetite on the sample surface[50,51].

233

Figure 1. XPS wide energy scans acquired before (black) and after (red) the ablation process of the olivine single crystal. Dashed lines highlight the features related to Auger electron emission.
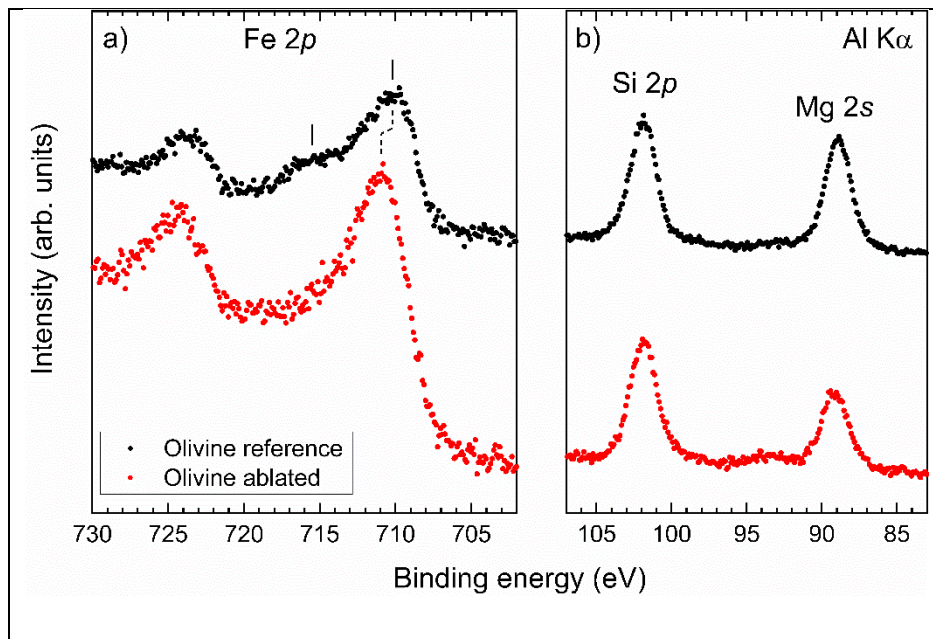
234

Figure 2. XPS spectra acquired on the a) Fe 2*p* and b) Si 2*p* and Mg 2*s* energy regions before (black) and after (red) the ablation process. Spectra have been normalized to the Si 2*p* photoemission intensity. Vertical lines in panel a) mark the energy position of the Fe 2*p*3/2 photoemission peak and its satellite.

235

236

237

238   **Optical absorption spectroscopy**

239   Optical absorption measurements on the resulting colloidal suspension composed by the

240   material ejected from the olivine surface into the water show a main band around 218 nm. This

241   feature is very similar to the "B_2 band" reported in several studies on silica glass [52,53] and ascribed

242   to oxygen vacancies. This band is also a common feature in colloidal suspensions of synthetic

243   forsterite, Mg/Al-hydroxides and chrysotile. Notably, the band peak is subjected to a slight shift

244   due to the presence of different cationic species in addition or in substitution to silicon. In

245   particular, the main absorption signal shows a gradual shift from 217 nm (silica mesostructured

246   nanoparticles suspension signal) to about 218-219 nm when colloidal suspensions of synthetic

247   forsterite, ablated olivine nanoparticles and chrysotile are measured. While the shift is larger when

248   Mg- (222 nm) and Al- hydroxides (224 nm) are analysed (see Figure S2). Therefore, this behavior

249   suggests a dependance of the signal on both the coordination and valence of the cation species.

250   Moreover, the colloidal solution of olivine ejecta shows an additional and characteristic absorption

251   band around 270 nm, which is sensitive to pH. Indeed, it shifts progressively to 300 nm as the pH

252   is reduced by the addition of a diluted solution of sulfuric acid (Figure S3). This signal could be

253   due to the presence of SiO_2 nanoparticles together with ferric and ferrous oxides. These latter are

254   dissolved by sulfuric acid liberating ferric and ferrous ions which, at acidic pH, give rise to

255   absorption bands centered at 300 nm (see ref [54] SiO_2 nanoparticles; see refs [55,56] for magnetite

256   nanoparticles and [57]).

257

258   **High-resolution transmission electron microscopy**

259   After the LP-PLA and optical spectroscopy analyses, the colloidal suspension was (i) drop-

260   casted (2μl) onto a C-coated Cu grids and (ii) subjected to a drying process and re-dispersion in

261   ethanol for the application of a constant electric field to promote electro-deposition of suspended

262   nanoparticles onto C-coated Cu grids serving as anode and cathode. These grids were then

263   analyzed by means of HR-TEM/EDS.

264   **Drop-cast grid**

265   Detailed HR-TEM imaging analyses on the drop-cast of the ejecta revealed the structural

266   complexity of the ablated material. The size distribution varies from large globular aggregates of

267   hundreds of nanometers in diameters (~600 nm) to small nanoparticles of 4-10 nm in diameter

268   (Figure 3 a-f) as also confirmed by the DLS analyses (see Figure S4). Moreover, large crystalline

269   fragments of hundreds of nanometers are also present (Figure3 g-i).
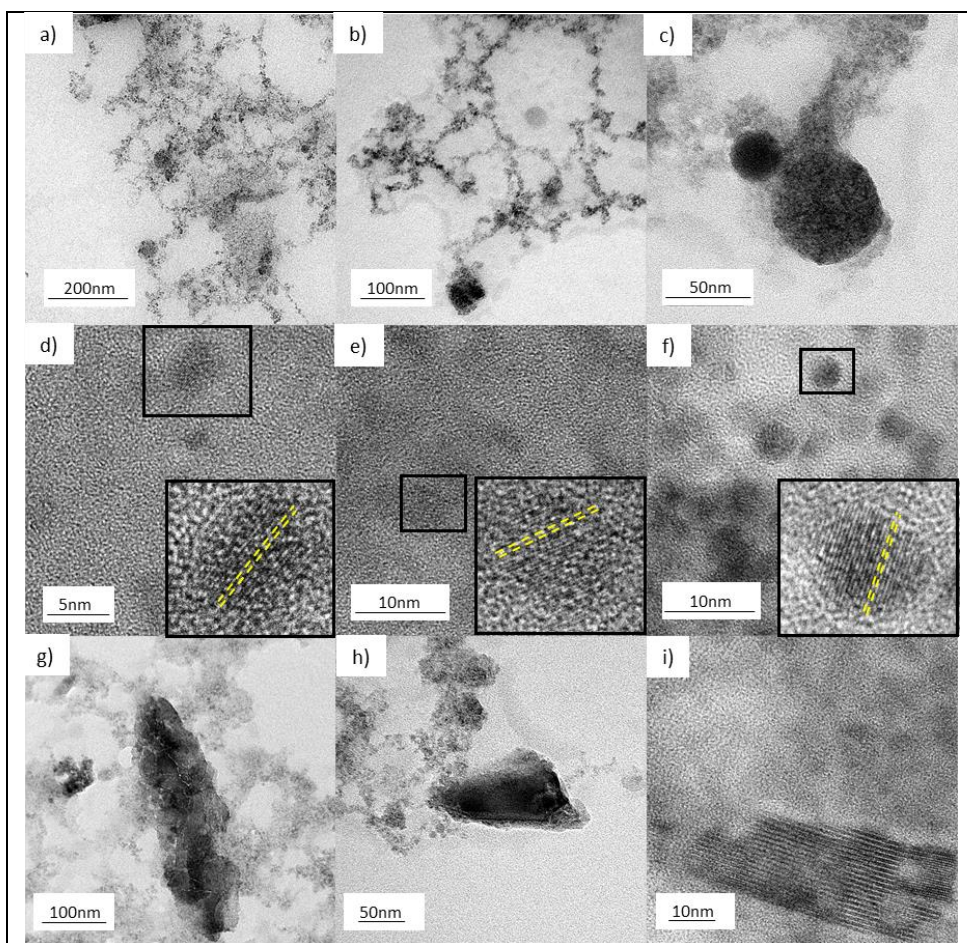
270

14

Figure 3. Bright field images of the drop-cast colloidal suspension: (a,b,c) Globular nanoparticle aggregates; (d,e,f) high-resolution images of the aggregates in (a) showing the individual nanoparticles of about 4 to 10 nm in diameter and their lattice fringes as evident in the insets; (g,h,i) crystalline fragments.

271

272   High-resolution bright field images were collected in the region nearby the globular

273 aggregates (as those reported in Figure 3 a-c) revealing the presence of spherical particles at the

274 nanoscale (see Figure 3 d-f). The nanoparticles show evidence of lattice fringes pointing to their

275 crystalline nature. Because of the low concentration of nanoparticles within the selected area

276 aperture, their very small dimensions, and the high background due to the carbon membrane and

277 amorphous material in general, diffraction rings were discontinuous and diffuse, and could not be

278 profitably exploited. The interplanar distances of the crystalline nanoparticles were therefore

279 obtained by the lattice fringe spacing in high-resolution images, which gave a systematic value

280 around 2.1 ± 0.1 Å (value averaged on 12 measurements). Unfortunately, this datum alone was not

281 sufficient to univocally identify the nanoparticles, since most candidate phases have at least one

282 family of crystallographic planes with distances in this range. EDS spectra collected on the

283 nanoparticle aggregates show the presence of Fe, Mg, Si and O with sometimes a slight enrichment

284 in Fe with respect to Mg, indicating a compositional change of the nano-ablated product with

285 respect to the parent olivine (see Figure S5). On this basis, and considering the measured average

286 d-spacing of 2.1 ± 0.1 Å, periclase (most intense reflection at 2.11 Å) and wustite (most intense

287 reflection at 2.15 Å) are among the possible phases forming the ejecta material.

288 On the other hand, the average measurable interlayer spacings of the large fragment

289 displayed in Figure 3i are 10.2(3) Å and 4.8(2) Å, which are consistent with (010) and (100) planes

290 of olivine, respectively (Figure 4a). This same fragment also shows some clear effects of the

291 ablation process such as local lack of periodicity and misorientation of the lattice planes (see Figure

292 4a). These features, along with the resulting EDS spectrum (Figure 4b), are consistent with

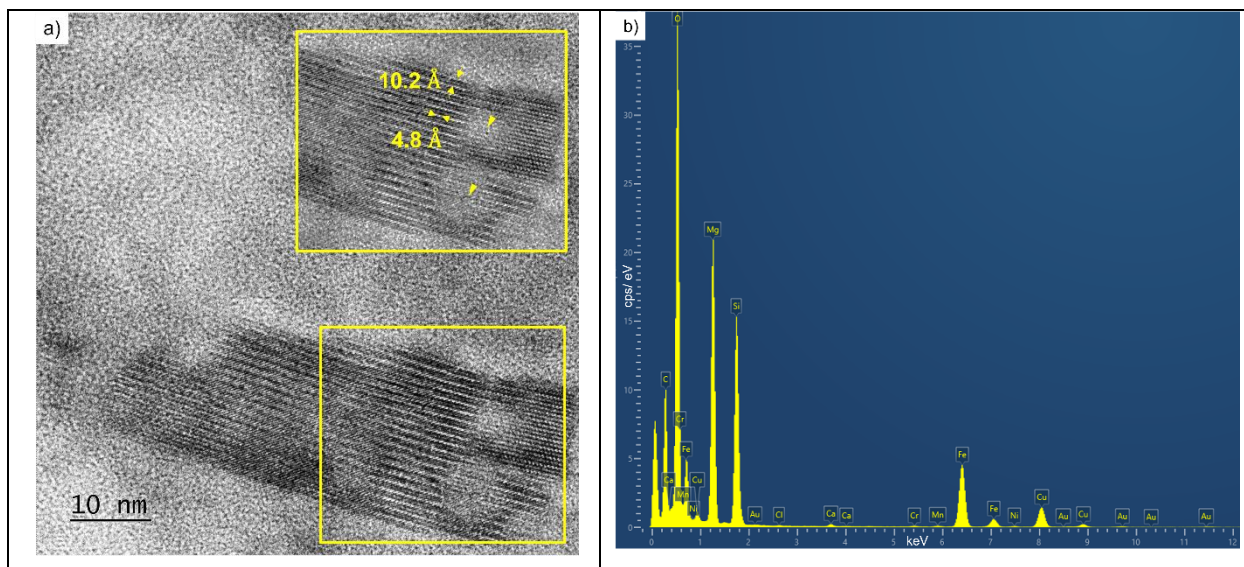293 fragments of ablated olivine.

16

Figure 4. a) Large crystalline fragment found in the ablated product. It shows d-spacings of 10.2(3) and 4.8(2) Å consistent with the (010) and (100) planes of olivine, view along [001]. Effects of the ablation process are also evident as planes misorientation and lack of periodicity (yellow arrows in the top right inset). **b)** EDS spectrum.

Electro-deposition grids

Electro-deposition was performed in order to exploit the electrostatic properties of the suspended nanoparticles with the aim to promote their separation and, consequently, to allow for a better chemical characterization. The analysis of the ζ-potential of the ablated nanoparticles re-suspended in ethanol performed by dynamic light scattering methods showed a clear population of charged particles centered at −30 mV (see Figure S6). Despite this evidence, after electro-deposition, nanoparticles were revealed in both the cathode and anode C- coated Cu grids (Figure 5). Moreover, the electro-deposition promoted the formation of a homogeneous layer of nanoparticles with sometimes sparse branched big aggregates (see Figure S7).

17

304   On the cathode, nanoparticles are found with an average diameter size of 4 ± 1 nm, while

305   on the anode the size of the nanoparticle was 9 ± 3 nm (Figure 5a and c). The nanoparticles on

306   both the electrodes give neater signals with respect to those of the drop-cast allowing for a
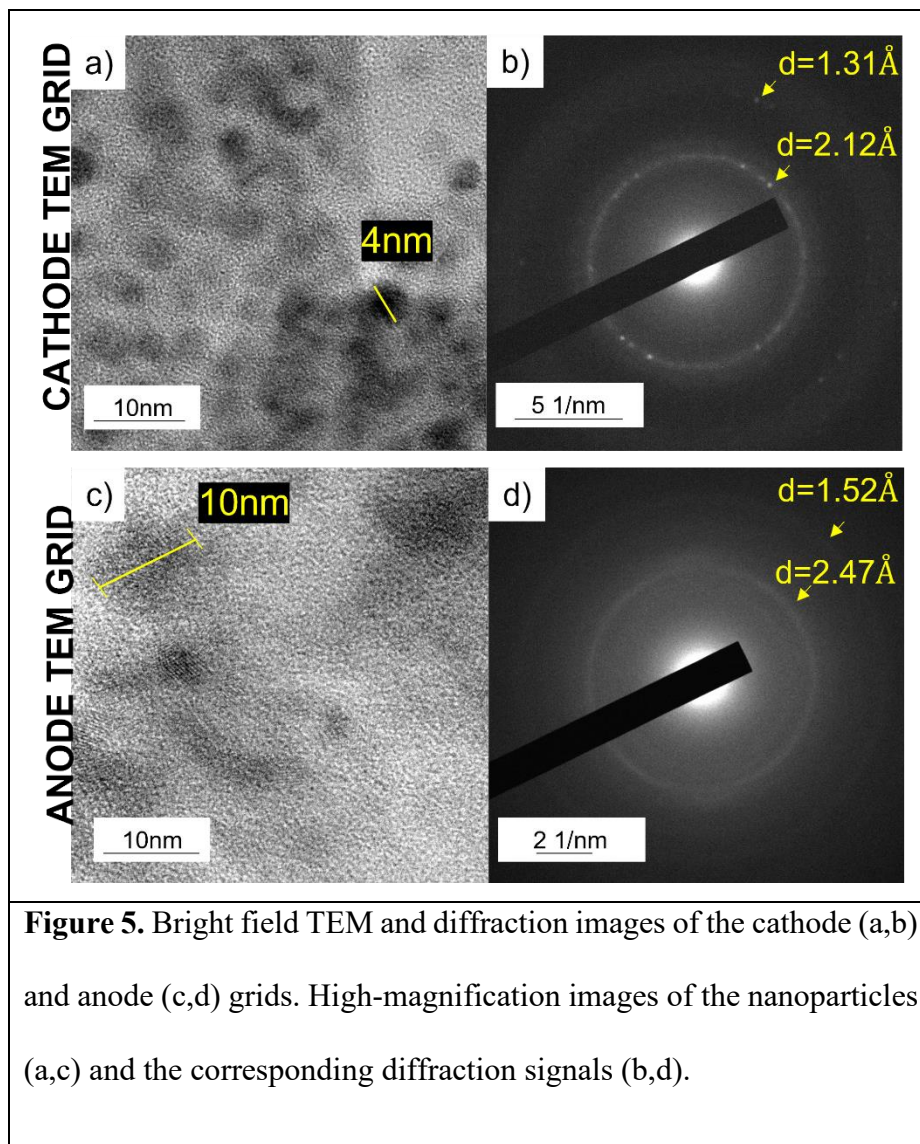
307   diffraction analysis.

308   The SAED patterns acquired on the nanoparticle aggregates reported in Figure 5b and d

309   show the coexistence of an amorphous fraction (diffuse haloes) together with a crystalline one

310   (weak diffraction rings and spotted rings, see yellow arrows). Interlayer spacings of the crystalline

311   nanoparticles have been determined from (i) HR lattice fringe images and (ii) SAED patterns.

312   Among all the measured values four main d-spacings have been measured: 1.32 ± 0.01 Å (average

313   of 2 measurements), 1.60 ± 0.01 Å (average over 3 measurements), 2.13 ± 0.06 Å (average of 44

314   measurements) and 2.52 ± 0.05 Å (average of 17 measurements). Moreover, in high-resolution

315   bright-field images, each individual crystalline nanoparticle shows only one lattice fringe

316   corresponding to one of the four aforementioned d-spacings, while in the collected SAED patterns

317   up to two simultaneous reflections among the four reported above can be observed (see yellow

318   arrows in Figure 5b and d). The measured interlayer spacings are consistent with the most intense

319   X-ray reflections of wustite, periclase, metallic Mg, magnetite, hematite, magnesioferrite and

320   maghemite (see highlighted values in Table S2). The diffuse haloes are located close to the

321   diffraction rings and have average d-spacings of 2.1 ± 0.1 Å, 1.2 ± 0.2 Å (Figure 5b) and 2.5 ± 0.1

322   Å, 1.56 ± 0.2 Å (Figure 5d), similar to those measured for the crystalline fraction [58,59].

323   Therefore, in order to narrow the range of the possible phases, we collected EDS spectra

324   on both the electrodes in areas with a sufficient concentration of nanoparticles. The chemical

325   analyses revealed the presence of only Mg, Si and O, whereas Fe was below the detection limit

326   (see Figure S8). The higher amount of Mg with respect to Fe together with the measured d-spacings

327   point out to a possible presence of periclase nanoparticles as dominant phase in the ejecta material.

328   Furthermore, it is worth noting that, despite showing the same morphology and chemical

329   composition, the nanoparticles were found with smaller size on the cathode, while with larger size

330   on the anode. This points to a dependence of the nanoparticle charge on its size due to their high

331   surface-to-volume ratio [40,60,61].

332

Figure 5. Bright field TEM and diffraction images of the cathode (a,b) and anode (c,d) grids. High-magnification images of the nanoparticles (a,c) and the corresponding diffraction signals (b,d).

333

334

335   DISCUSSION

336   Our multi methodological approach, combining the analysis of both the ablated material

337   and the target, showed the occurrence of clear structural and chemical changes as a consequence

338   of the simulation of space weathering in water environment. Specifically, the ablated material

339   (ejecta) is made up by (i) a fraction of crystalline nanoparticles (4-10 nm in diameter) with

340   diffraction signals mostly compatible with the presence of metallic Mg and/or periclase as the

341   dominant phase with minor Fe-oxides; (ii) amorphous material (as evident from the diffuse halo

342   in the diffraction images) with a composition close to the crystalline fraction and (iii) shocked

343   crystalline olivine fragments of size of the order of 500-600 nm (see Figure 3 g-I and Figure 4).

344   On the other hand, the target is depleted in Mg and enriched in Fe, showing a partial

345   oxidation of Fe^{2+} into Fe^{3+}, in agreement with the formation of magnetite domains on the sample

346   surface.

347   The evidence of partial oxidation of Fe^{2+} into Fe^{3+} on the target surface is in net contrast

348   with the results of similar ablation experiments on olivine samples performed in vacuum [17,18,22],

349   where the authors report the occurrence of metallic Fe-nanoparticles. The presence of metallic iron

350   particles together with the Mg removal from the target is explained by the thermal reduction

351   mechanism in absence of a subsequent re-oxidation (see ref [22] for more details). Chemical

352   reduction is a common process also in water, promoted by hydrated electrons forming during

353   plasma ignition which are potentially able to reduce both Fe and Mg into their metallic state [40].

354   These species might survive in water (or even only in air) as nanoparticles only if immediately

355   capped by an inert layer. This layer has been demonstrated to be represented by silica in laser

356   ablation experiments performed on Si targets immersed in metallic precursor solutions (Ag^+,

357 Au^{3+}). These studies have shown that metastable species such as H_2SiO_2 can be formed as the

358 result of the interaction of Si-rich targets and water, exhibiting the capability of reducing noble

359 metal ions into metallic nanoparticles while oxidizing into silica forming a capping layer around

360 them [57,62-66]. In our case, this process might be active in a region relatively far from the solid-liquid

361 interface, while re-oxidation is promoted by the presence of radical species in the water

362 environment in a region confined at the solid-liquid interface [67]. This might account for the fact

363 that we have nanoparticles compatible with metallic Mg. However, by the analysis of the lattice

364 spacing of the produced nanoparticles, we can confidently rule out the presence of metallic Fe.

365 This observation can be explained by an apparent tendency of Fe-ions to remain bonded to the

366 target, in contrast to the tendency of Mg-ions to detach from the target, as demonstrated by the

367 increase in the Fe-related signal and the simultaneous decrease in the Mg-related signal in XPS

368 spectra (Figure 2).

369   Since the raster scanning of the target during the ablation process was performed by

370 moving the stage manually, it is likely that the newly formed magnetite on the sample surface was

371 also subjected to a subsequent ablation with its further transport into the colloidal suspension.

372 Indeed, the measured spacings of the crystalline nanoparticles are also consistent with the presence

373 of magnetite, in addition to the other abovementioned possible Mg and Fe phases (see TEM results

374 session). However, the presence of Fe has been detected only in the drop-cast material, while it

375 was below the detection limit on both cathode and anode grids (Figure S8). Therefore, the d-

376 spacings measured on both cathode and anode TEM grids, even if compatible with the presence of

377 magnetite and other Fe compounds (see Table S2), are likely due to Mg compounds (i.e., silica-

378 capped metallic Mg and periclase). This evidence indicates that Fe-bearing nanoparticles do not

379   acquire a substantial charge enabling their migration to the electrodes when re-dispersed in
380   ethanol.

381   The presence of iron oxides (e.g., magnetite) and therefore the absence of metallic iron is
382   consistent with an environment that experienced aqueous alteration during its history as occurred
383   for example on Mars or on carbonaceous chondrites parent body [68-71]. Moreover, in the outer space,
384   a large number of bodies is (or has been) characterized by the presence of volatile-rich elements
385   as well as hydrous minerals or water ices (e.g., Mars, Ceres, asteroids, comets) that affect the
386   chemistry and physics of space weathering processes [15,29,72]. In particular, magnetite is quite
387   ubiquitous on Earth and in planetary materials and it is often a marker for a variety of processes
388   as for water-rock interactions (e.g., serpentinization, see ref [73] and references therein).

389

390

391   CONCLUSIONS

392   The coupling of the nanosecond liquid-phase pulsed laser ablation with the use of olivine
393   single crystals as targets allows us to characterize both the shocked target and the ejecta material
394   (i.e., colloidal suspension).

395   We provide a methodological approach to investigate space weathering processes in a
396   water environment. We observed that the water environment triggers the partial oxidation of Fe^{2+}
397   into Fe^{3+} in a region confined at the solid target-liquid interface, promoting the formation of
398   magnetite on the sample surface. On the other hand, Mg is easily removed, and the target results
399   Mg-depleted (Fe-enriched) after the ablation process.

400   In the ablated material, we find crystalline fragments close to an olivine composition (i.e.,
401   starting material) together with amorphous and crystalline nanoparticles. The crystalline

402   nanoparticles have diffraction signals compatible with the mainly occurrence of Mg- bearing

403   phases (i.e., Mg metallic and periclase) with minor Fe- phases: from silica-capped metallic Mg to

404   magnetite. The latter probably coming from the ablation of the newly oxidized iron at the solid-

405   liquid interface. The diffuse diffraction signals present in the diffraction images (Figure 5) together

406   with the EDS analyses are also consistent with the occurrence of the same phases, as reported

407   above for the crystalline nanoparticles, but in an amorphous status.

408   The identification of magnetite on the olivine surface together with the occurrence of iron

409   oxides and metallic Mg capped by a silica shell in the ablated material might represent evidence

410   of a space weathering processes associated with an aqueous environment on planetary materials

411   and asteroids. Moreover, it seems clear that iron has a weak tendency to escape the olivine surface

412   and that the water environment triggers its oxidation. This is expected to affect reflectance spectra

413   through the absence of features related to metallic iron nanoparticles and the lack of reddening

414   phenomena. Moreover, this has profound implications in several research fields from astrobiology

415   to planetary geology.

416   Even if a lot of work is still required to better identify the ablated species in the ejecta

417   material, we provide an unexplored procedure in the field of space weathering studies of

418   astronomical silicates. This study also contributes to the development of the new research area

419   focused on the study of space weathering and alteration processes in different environments with

420   respect to those of the airless silicate bodies in the inner solar system.

421

422

423

424

425 ASSOCIATED CONTENT

426 **Supporting Information**

427 The Supporting Information is available free of charge at:

428 Chemical analyses (Table S1), Mössbauer spectra (Figure S1), Absorption spectra (Figure S2),

429 Absorption spectra with addition of known aliquots of sulfuric acid (Figure S3), Dynamic light

430 scattering measurements (Figure S4), TEM/EDS chemical analyses (Figure S5), Zeta potential

431 measurement (Figure S6), Low magnification TEM images (Figure S7), d-spacing of reference

432 chemical species (Table S2), EDS spectra (Figure S8) (PDF)

433

434

435 AUTHOR INFORMATION

436 **Corresponding Author**

437 Marcello Campione – Department of Earth and Environmental Sciences, University of Milano-

438 Bicocca, I-20126 Milano, Italy;

439 **Email:** marcello.campione@unimib.it

440 **Authors**

441 **Mara Murri -** *Department of Earth and Environmental Sciences, University of Milano-Bicocca,*

442 *I-20126 Milano, Italy*

443 **Giancarlo Capitani -** *Department of Earth and Environmental Sciences, University of Milano-*

444 *Bicocca, I-20126 Milano, Italy*

445 **Mauro Fasoli -** *Department of Materials Science, University of Milano - Bicocca, I-20125 Milano,*

446 *Italy*

447 **Angelo Monguzzi -** *Department of Materials Science, University of Milano - Bicocca, I-20125*
448 *Milano, Italy*

449 **Alberto Calloni -** *Department of Physics, Politecnico di Milano, I-20133 Milano, Italy*

450 **Gianlorenzo Bussetti -** *Department of Physics, Politecnico di Milano, I-20133 Milano, Italy*

451 **Nadia Malaspina -** *Department of Earth and Environmental Sciences, University of Milano-*
452 *Bicocca, I-20126 Milano, Italy*

453 **Notes**

454 The authors declare no competing financial interest.

463

464

465

466

467

468 REFERENCES

469   (1)   Saunders, R.W.; Plane, J. M. A photo-chemical method for the production of olivine

470   nanoparticles   as   cosmic   dust   analogues.   *Icarus*   **2011**,   *212*,   373-382,

471   DOI:10.1016/j.icarus.2010.12.019.

472   (2)   Ysard, N.; Jones, A. P.; Demyk, K.; Boutéraon, T.; Koehler, M. The optical properties of

473   dust: the effects of composition, size, and structure. *Astronomy & Astrophysics* **2018**, *617*,

474   DOI:10.1051/0004-6361/201833386.

475   (3)   Hochella, M.F.; Lower, S. K.; Maurice, P. A.; Penn, R. L.; Sahai, N.; Sparks, D. L.;

476   Twining, B. S. Nanominerals, mineral nanoparticles, and earth systems. *Science* **2008**, *319*, 1631-

477   1635, DOI:10.1126/science.1141134.

478   (4)   Signorile, M.; Zamirri, L.; Tsuchiyama, A.; Ugliengo, P.; Bonino, F.;Martra, G. On the

479   Surface Acid–Base Properties of Amorphous and Crystalline Mg_2SiO_4 as Probed by Adsorbed

480   CO, CO_2,   and   CD3CN.   *ACS   Earth   Space   Chem.*   **2020**,   *4*,   345-354,

481   DOI:10.1021/acsearthspacechem.9b00271.

482   (5)   Witt, A.N. Small and very small interstellar grains. *J. Geophys. Res. Space Phys.* **2000**,

483   *105*, 10299-10302, DOI:10.1029/1999JA900208.

484   (6)   Li,   A.   Cosmic   crystals   caught   in   the   act.   *Nature*   **2009**,   *459*,   173-175,

485   DOI:10.1038/459173a.

486   (7)   Escatllar, A.M.; Lazaukas, T.; Woodley, S. M.; Bromley, S. T. Structure and properties of

487   nanosilicates with olivine (Mg_2SiO_4) N and pyroxene ($MgSiO_3$) N compositions. *ACS Earth Space*

488   *Chem.* **2019**, *3*, 2390-2403, DOI:10.1021/acsearthspacechem.9b00139.

489   (8)   Kamijo, F. A theoretical study on the long period variable star, III. formation of solid or

490   liquid particles in the circumstellar envelope. *Publications of the Astronomical Society of Japan*

491   *15* **1963.**

492   (9)   Li, A.; Draine, B. T. On ultrasmall silicate grains in the diffuse interstellar medium. *ApJ*

493   *Letters* **2001**, *550*, DOI:10.1086/319640.

494   (10) Carrez, P.; Demyk, K.; Cordier, P.; Gengembre, L.; Grimblot, J.; D'Hendecourt, L.; Jones,

495   A.P;Leroux, H. Low-energy helium ion irradiation-induced amorphization and chemical changes

496   in olivine: Insights for silicate dust evolution in the interstellar medium. *Meteorit. Planet. Sci.*

497   **2002**, *37*, 1599-1614, DOI:10.1111/j.1945-5100.2002.tb00814.x.

498   (11) Zamirri, L.; Macia Escatllar, A.; Mariñoso Guiu, J.; Ugliengo, P.; Bromley, S. T. What

499   Can Infrared Spectra Tell Us about the Crystallinity of Nanosized Interstellar Silicate Dust Grains?

500   *ACS Earth and Space Chem.* **2019**, *3*, 2323-2338, DOI:10.1021/acsearthspacechem.9b00157

501   (12) Henning, T. Cosmic silicates. *Annu. Rev. Astron. Astrophys.* **2010**, *48*, 21-46,

502   DOI:10.1146/annurev-astro-081309-130815.

503   (13) Draine, B.T.; Lee, H. M. Optical properties of interstellar graphite and silicate grains. *ApJ*

504   **1984**, *285*, 89-108., DOI: 10.1086/162480.

505   (14) Fogerty, S.; Forrest, W.; Watson, D. M.; Sargent, B. A.; Koch, I. Silicate composition of

506   the interstellar medium. *ApJ* **2016**, *830*, DOI:10.3847/0004-637X/830/2/71.

507

508   (15) Pieters, C.M.; Noble, S. K. Space weathering on airless bodies.   *J.   Geophys.   Res.*

509   *Planets* **2016**, *121*, 1865-1884, DOI:10.1002/2016JE005128.

510   (16) Sasaki, S.; Nakamura, K.; Hamabe, Y.; Kurahashi, E.; Hiroi, T. Production of iron

511   nanoparticles by laser irradiation in a simulation of lunar-like space weathering. *Nature* **2001**, *410,*

512   555-557, DOI:10.1038/35069013.

513   (17) Loeffler, M.J.; Baragiola, R. A.; Murayama, M. Laboratory simulations of redeposition of

514   impact ejecta on mineral surfaces. *Icarus* **2008**, *196*, 285-292, DOI:10.1016/j.icarus.2008.02.021.

515   (18) Loeffler, M.J.; Dukes, C. A.; Christoffersen, R.; Baragiola, R. A. Space weathering of

516   silicates simulated by successive laser irradiation: In situ reflectance measurements of Fo90,

517   Fo99+, and SiO_2. *Meteorit. Planet. Sci.* **2016**, *51*, 261-275, DOI:10.1111/maps.12581.

518   (19) Thompson, M.S.; Loeffler, M. J.; Morris, R. V.; Keller, L. P.; Christoffersen, R. Spectral

519   and chemical effects of simulated space weathering of the Murchison CM2 carbonaceous

520   chondrite. *Icarus* **2019**, *319*, 499-511, DOI:10.1016/j.icarus.2018.09.022.

521   (20) Dukes, C.A.; Baragiola, R. A.; McFadden, L. A. Surface modification of olivine by H+

522   and He+ bombardment. *J. Geophys. Res. Planets* **1999**, *104*, 1865-1872, DOI:10.1029/98JE02820.

523   (21) Zamirri, L.; Corno, M.; Rimola, A.; Ugliengo, P.Forsterite surfaces as models of

524   interstellar core dust grains: computational study of carbon monoxide adsorption. *ACS Earth Space*

525   *Chem.* **2017**, *1*, 384-398, DOI:10.1021/acsearthspacechem.7b00041.

526   (22) Fazio, A.; Harries, D.; Matthäus, G.; Mutschke, H.; Nolte, S.;Langenhorst, F. Femtosecond

527   laser irradiation of olivine single crystals: Experimental simulation of space weathering. *Icarus*

528   **2018**, *299*, 240-252, DOI:10.1016/j.icarus.2017.07.025.

529 (23) Guiu, J.M.; Escatllar, A. M.; Bromley, S. T. How Does Temperature Affect the Infrared

530 Vibrational Spectra of Nanosized Silicate Dust? *ACS Earth Space Chem.* **2021**, *5*, 812-823,

531 DOI:10.1021/acsearthspacechem.0c00341.

532 (24) Sasaki, S.; Kurahashi, E.; Yamanaka, C.; Nakamura, K. Laboratory simulation of space

533 weathering: Changes of optical properties and TEM/ESR confirmation of nanophase metallic iron.

534 *Adv. Space Res.* **2003**, *31*, 2537-2542, DOI:10.1016/S0273-1177(03)00575-1.

535 (25) Fazio, A.; Matthäus, G.; Harries, D.; Mutschke, H.; Nolte, S.; Langenhorst, F. Reproducing

536 space weathering of olivine by using high-energy femtosecond laser pulses. *In Frontiers in*

537 *Ultrafast Optics: Biomedical, Scientific, and Industrial Applications XVII. International Society*

538 *for Optics and Photonics.* **2017**, *10094*, DOI:10.1117/12.2252130.

539 (26) Schmidt, D.; Pollok, K.; Matthäus, G.; Nolte, S.; Langenhorst, F. Nanodeformation in

540 enstatite single crystals: Simulation of micrometeoroid impacts by femtosecond pulsed laser

541 experiments. . *Geochemistry* **2019**, *79*, DOI:10.1016/j.chemer.2019.125542.

542 (27) Campins, H.; Hargrove, K.; Pinilla-Alonso, N.; Howell, E.S.; Kelley, M.S.; Licandro, J.;

543 Mothé-Diniz, T.; Fernández, Y.; Ziffer, J. Water ice and organics on the surface of the asteroid 24

544 Themis. *Nature* **2010**, *464*, 1320-1321, DOI:10.1038/nature09029.

545 (28) Rivkin, A.S.; Emery, J. P. Detection of ice and organics on an asteroidal surface. *Nature*

546 **2010**, *464*, 1322-1323, DOI:10.1038/nature09028.

547 (29) Blewett, D.T.; Denevi, B.W.; Le Corre, L.; Reddy, V.; Schröder, S.E.; Pieters, C.M.; Tosi,

548 F.; Zambon, F.; De Sanctis, M.C.; Ammannito, E.;Roatsch, T. Optical space weathering on Vesta:

549   Radiative-transfer   models   and   Dawn   observations. *Icarus* **2016**, *265*, 161-174,

550   DOI:10.1016/j.icarus.2015.10.012.

551   (30) Bu, C.; Lopez, G. R.; Dukes, C. A.; McFadden, L. A.; Li, J. Y.; Ruesch, O. Stability of

552   hydrated carbonates on Ceres. *Icarus* **2019**, *320*, 136-149, DOI:10.1016/j.icarus.2017.12.036.

553   (31) Brownlee, D. et al. Comet 81P/Wild 2 Under a Microscope. *Science* **2006**, *314*, DOI:

554   10.1126/science.1135840.

555   (32) Fulle, M.B., J. Fractal dust constrains the collisional history of comets. *Monthly Notices of*

556   *the Royal Astronomical Society,* **2017**, *469*, DOI: 10.1093/mnras/stx971.

557   (33) Potapov, A.; Mutschke, H.; Seeber, P.; Henning, T.; Jäger, C. Low-temperature Optical

558   Properties of Interstellar and Circumstellar Icy Silicate Grain Analogs in the Mid-infrared Spectral

559   Region. *ApJ* **2018**, *861*, DOI:10.3847/1538-4357/aac6d3.

560   (34) Potapov, A.; Jäger, C.; Henning, T. Temperature programmed desorption of water ice from

561   the surface of amorphous carbon and silicate grains as related to planet-forming disks. *ApJ* **2018**,

562   *865*, DOI:10.3847/1538-4357/aad803.

563   (35) Draine, B.T. Interstellar Dust Grains. *Annu. Rev. Astron. Astrophys.* **2003**, *41*, 241-289,

564   DOI:10.1146/annurev.astro.41.011802.094840.

565   (36) Patil, P.P.; Phase, D.M.; Kulkarni, S.A.; Ghaisas, S.V.; Kulkarni, S.K.; Kanetkar, S.M.;

566   Ogale, S.B.;Bhide, V.G. Pulsed-laser–induced reactive quenching at liquid-solid interface:

567   Aqueous oxidation of iron. *Phys. Rev. Lett.* **1987**, *58*, DOI:10.1103/PhysRevLett.58.238.

568   (37) Kanitz, A.; Kalus, M.R.; Gurevich, E.L.; Ostendorf, A.; Barcikowski, S.; Amans, D.

569   Review on experimental and theoretical investigations of the early stage, femtoseconds to

570   microseconds processes during laser ablation in liquid-phase for the synthesis of colloidal

571   nanoparticles. *Plasma Sources Sci. Technol.* **2019**, *28*, DOI:10.1088/1361-6595/ab3dbe.

572   (38) Shih, C.Y.; Shugaev, M.V.; Wu, C.; Zhigilei, L.V. The effect of pulse duration on

573   nanoparticle generation in pulsed laser ablation in liquids: insights from large-scale atomistic

574   simulations. *Phys. Chem. Chem. Phys.* **2020**, *22*, 7077-7099, DOI:10.1039/d0cp00608d.

575   (39) Tabata, H.; Fujii, M.; Hayashi, S.; Doi, T.; Wakabayashi, T. Raman and surface-enhanced

576   Raman scattering of a series of size-separated polyynes. *Carbon* **2006**, *44*, 3168-3176,

577   DOI:10.1016/j.carbon.2006.07.004.

578   (40) Chen, Q.; Li, J.; Li, Y. A review of plasma–liquid interactions for nanomaterial synthesis.

579   *J. Phys. D Appl. Phys.* **2015**, *48*, DOI:10.1088/0022-3727/48/42/424005.

580   (41) Svetlichnyi, V.A.; Shabalina, A.V.; Lapin, I.N.; Goncharova, D.A.; Kharlamova, T.S.;

581   Stadnichenko, A.I. Comparative study of magnetite nanoparticles obtained by pulsed laser ablation

582   in water and air. *Appl. Surf. Sci.* **2019**, *467-468*, 402-410, DOI:10.1016/j.apsusc.2018.10.189.

583   (42) Beier, C.; Haase, K.M.; Hansteen, T.H. Magma Evolution of the Sete Cidades Volcano,

584   São Miguel, Azores. *J. Petrol.* **2006**, *47*, 1375-1411, DOI:10.1093/petrology/egl014.

585   (43) Rüffer, R.; Chumakov, A. I. Nuclear resonance beamline at ESRF. *Hyperfine Interact.*

586   **1996**, *97*, 589-604, DOI:10.1007/BF02150199.

587 (44) Potapkin, V.; Chumakov, A. I.; Smirnov, G. V.; Celse, J. P.; Rüffer, R.; McCammon, C.;

588 Dubrovinsky, L. The 57Fe synchrotron Mössbauer source at the ESRF. *Journal of synchrotron*

589 *radiation* **2012**, *19*, 559-569., DOI:10.1107/S0909049512015579.

590 (45) Prescher, C.; McCammon, C.; Dubrovinsky, L. MossA: a program for analyzing energy-

591 domain Mössbauer spectra from conventional and synchrotron sources. *J. Appl. Crystallogr.* **2012**

592 *45*, 329-331, DOI:10.1107/S0021889812004979.

593 (46) Berti, G.; Calloni, A.; Brambilla, A.; Bussetti, G.; Duo, L.; Ciccacci, F. Direct observation

594 of spin-resolved full and empty electron states in ferromagnetic surfaces. *Rev. Sci. Instrum.* **2014**,

595 *85*, DOI:10.1063/1.4885447.

596 (47) Mitchell, D.R.G. DiffTools: Electron Diffraction Software Tools for DigitalMicrograph[TM].

597 *Microsc. Res. Tech.* **2008** *71,*588-593, DOI: 10.1002/jemt.20591.

598 (48) Calloni, A.; Berti, G.; Brambilla, A.; Riva, M.; Picone, A.; Bussetti, G.; Finazzi, M.;

599 Ciccacci, F.; Duo, L. Electron spectroscopy investigation of the oxidation of ultra-thin films of Ni

600 and Cr on Fe(0 0 1). *J Phys Condens Matter* **2014**, *26*, 445001, DOI:10.1088/0953-

601 8984/26/44/445001.

602 (49) Brambilla, A.; Calloni, A.; Berti, G.; Bussetti, G.; Duò, L.; Ciccacci, F. Growth and

603 Interface Reactivity of Titanium Oxide Thin Films on Fe(001). *J. Phys. Chem. C.* **2013**, *117*, 9229-

604 9236, DOI:10.1021/jp400159j.

605 (50) Gota, S.; Guiot, E.; Henriot, M.; Gautier-Soyer, M. Atomic-oxygen-assisted MBE growth

606 of $\alpha-$ Fe_2O_3 on $\alpha-$ Al_2O_3 (0001): Metastable FeO (111)-like phase at subnanometer thicknesses.

607 *Phys. Rev. B* **1999**, *60*, DOI:10.1103/PhysRevB.60.14387.

608   (51) Seyama, H.;Soma, M. Fe 2p spectra of silicate minerals. *J Electron Spectros. Relat.*

609   *Phenomena* **1987**, *42*, 97-101, DOI:10.1016/0368-2048(87)85010-7.

610   (52) Skuja, L.N.; Streletsky, A. N.; Pakovich, A. B. A new intrinsic defect in amorphous SiO2:

611   twofold coordinated silicon. *Solid state commun.* **1984**, *50*, 1069-1072, DOI:10.1016/0038-

612   1098(84)90290-4.

613   (53) Tohmon, R.; Mizuno, H.; Ohki, Y.; Sasagane, K.; Nagasawa, K.; Hama, Y. Correlation of

614   the 5.0- and 7.6-eV absorption bands in SiO_2 with oxygen vacancy. *Phys. Rev. B Condens. Matter*

615   **1989**, *39*, 1337-1345, DOI:10.1103/physrevb.39.1337.

616   (54) Rawat, R.; Tiwari, A.; Vendamani, V.S.; Pathak, A.P.; Rao, S.V.; Tripathi, A. Synthesis

617   of Si/SiO_2 nanoparticles using nanosecond laser ablation of silicate-rich garnet in water. *Opt.*

618   *Mater.* **2018**, *75*, 350-356, DOI:10.1016/j.optmat.2017.10.045.

619   (55) Wang, Y.; Xu, C.; Chang, Y.; Zhao, L.; Zhang, K.; Zhao, Y.; Gao, F.; Gao, X. Ultrasmall

620   superparamagnetic iron oxide nanoparticle for T 2-weighted magnetic resonance imaging. *ACS*

621   *Appl. Mater. Interfaces* **2017**, *9*, 28959-28966, DOI:10.1021/acsami.7b10030.

622   (56) Roychowdhury, A.; Pati, S. P.; Kumar, S.; Das, D. Effects of magnetite nanoparticles on

623   optical properties of zinc sulfide in fluorescent-magnetic Fe_3O_4/ZnS nanocomposites. *Powder*

624   *Technol.* **2014**, *254*, 583-590, DOI:10.1016/j.powtec.2014.01.076.

625   (57) Loures, C.C.A.; Alcântara, M.A.K.; Filho, H.J.I.; Teixeira, A.C.S.C.; Silva, F.T.; Paiva,

626   T.C.B.; Samanamud, G.R.L. Advanced Oxidative Degradation Processes: Fundamentals and

627   Applications. *International Review of Chemical Engineering (IRECHE)* **2013**, *5*,

628   DOI:10.15866/ireche.v5i2.6909.

629   (58) Wang, L. M.; Ewing, R. C. Ion beam-induced amorphization of (Mg, Fe) 2SiO4 olivine

630   series: An in situ transmission electron microscopy study. *MRS Online Proceedings Library (OPL)*

631   **1991**, *235*. DOI:10.1557/PROC-235-333

632   (59) Wang, L. M.; Ewing, R. C. Ion-beam-induced amorphization of complex ceramic

633   materials—minerals. *MRS Bulletin* **1992**, *17*, 38-44. DOI:10.1557/S0883769400041270

634   (60) Barisik, M.; Atalay, S.; Beskok, A.; Qian, S. Size dependent surface charge properties of

635   silica nanoparticles. *J. Phys. Chem. C* **2014**, *118*, 1836-1842, DOI:10.1021/jp410536n.

636   (51) Shi, Y.R.; Ye, M. P.; Du, L. C.; Weng, Y. X. Experimental determination of particle size-

637   dependent surface charge density for silica nanospheres. *J. Phys. Chem. C* **2018**, *122*, 23764-

638   23771, DOI:10.1021/acs.jpcc.8b07566.

639   (62) McCarthy, M.C.; Gauss, J. Exotic SiO(2)H(2) Isomers: Theory and Experiment Working

640   in Harmony. *J. Phys. Chem. Lett.* **2016**, *7*, 1895-1900, DOI:10.1021/acs.jpclett.6b00632.

641   (63) Ermakov, V.A.; Jimenez-Villar, E.; Silva Filho, J.M.; Yassitepe, E.; Mogili, N.V.; Iikawa,

642   F.; de Sa, G.F.; Cesar, C.L.; Marques, F.C. Size Control of Silver-Core/Silica-Shell Nanoparticles

643   Fabricated by Laser-Ablation-Assisted Chemical Reduction. *Langmuir* **2017**, *33*, 2257-2262,

644   DOI:10.1021/acs.langmuir.6b04308.

645   (64) González-Castillo, J.R.; Rodríguez-González, E.; Jiménez-Villar, E.; Cesar, C.L.;

646   Andrade-Arvizu, J.A. Assisted laser ablation: silver/gold nanostructures coated with silica. *Appl.*

647   *Nanosci.* **2017**, *7*, 597-605, DOI:10.1007/s13204-017-0599-2.

648 (65) Hoang, H.T.; Sertsova, A.A.; Marakulin, S.I.; Subcheva, E.N.; Zaitseva, M.P.; Yurtov,

649 E.V. Manufacture of Magnesium Oxide Nanoparticles Coated with Silica Shells. *Russ. J. Inorg.*

650 *Chem.* **2018**, *63*, 1414-1418, DOI:10.1134/s0036023618110074.

651 (66) Livan, P.; Öztürk, T. Carbon encapsulation of elemental nanoparticles by spark discharge.

652 *J. Mater. Sci.* **2018**, *53*, 14350-14360, DOI:10.1007/s10853-018-2647-z.

653 (67) Broadhead, E.J.; Tibbetts, K.M. Fabrication of Gold-Silicon Nanostructured Surfaces with

654 Reactive Laser Ablation in Liquid. *Langmuir* **2020**, *36*, 10120-10129,

655 DOI:10.1021/acs.langmuir.0c01581.

656 (68) Ehlmann, B.L.; Mustard, J.F.; Murchie, S.L. Geologic setting of serpentine deposits on

657 Mars. *Geophys. Res. Lett.* **2010**, *37*, DOI:10.1029/2010gl042596.

658 (69) Lee, M.R.; Lindgren, P. Aqueous alteration of chondrules from the Murchison CM

659 carbonaceous chondrite: Replacement, pore filling, and the genesis of polyhedral serpentine.

660 *Meteorit. Planet. Sci.* **2016**, *51*, 1003-1021, DOI:10.1111/maps.12644.

661 (70) Veneranda, M.; Lopez-Reyes, G.; Pascual Sanchez, E.; Krzesinska, A.M.; Manrique-

662 Martinez, J.A.; Sanz-Arranz, A.; Lantz, C.; Lalla, E.; Moral, A.; Medina, J.; et al. ExoMars Raman

663 Laser Spectrometer: A Tool to Semiquantify the Serpentinization Degree of Olivine-Rich Rocks

664 on Mars. *Astrobiology* **2021**, *21*, 307-322, DOI:10.1089/ast.2020.2265.

665 (71) Smith, R.J.; McLennan, S.M.; Achilles, C.N.; Dehouck, E.; Horgan, B.H.N.; Mangold, N.;

666 Rampe, E.B.; Salvatore, M.; Siebach, K.L.; Sun, V. X-Ray Amorphous Components in

667 Sedimentary Rocks of Gale Crater, Mars: Evidence for Ancient Formation and Long-Lived

668 Aqueous Activity. *J. Geophys. Res. Planets* **2021**, *126*, DOI:10.1029/2020je006782.

669   (72) Potapov, A.; Bouwman, J.; Jäger, C.; Henning, T. Dust/ice mixing in cold regions and

670   solid-state water in the diffuse interstellar medium. *Nat. Astron.* **2021**, *5*, 78-85,

671   DOI:10.1038/s41550-020-01214-x.

672   (73) Izawa, M.R.M.; Cloutis, E.A.; Rhind, T.; Mertzman, S.A.; Applin, D.M.; Stromberg, J.M.;

673   Sherman, D.M. Spectral reflectance properties of magnetites: Implications for remote sensing.

674   *Icarus* **2019**, *319*, 525-539, DOI:10.1016/j.icarus.2018.10.002.

675

676

677

678